Influence of Stability and Surface Roughness on Turbulence during the Stable Atmospheric Variability and Transport (SAVANT) Field Campaign

SUDHEER R. BHIMIREDDY, A JUNMING WANG, APRIL L. HISCOX, AND DAVID A. R. KRISTOVICHA

^a Climate and Atmospheric Science Section, Division of State Water Survey, Prairie Research Institute, University of Illinois, Champaign, Illinois

^b Department of Geography, University of South Carolina, Columbia, South Carolina

(Manuscript received 9 August 2021, in final form 16 May 2022)

ABSTRACT: Harvesting of crops in a weakly sloping Midwestern field during the Stable Atmospheric Variability and Transport (SAVANT) observation campaign allowed for a systematic investigation of the influence of surface roughness and static stability magnitude on the applicability of the Monin–Obukhov similarity (MOST) and hockey-stick transition (HOST) theories during stable boundary layer periods. We analyze momentum flux and turbulent velocity scale $V_{\rm TKE}$ in three regimes, defined using the gradient Richardson number Ri and flux Richardson number Ri_f as regime 1 ($0 < {\rm Ri} \le 0.1$ and $0 < {\rm Ri}_f \le 0.1$), regime 2 ($0.1 < {\rm Ri} \le 0.23$ and $0.1 < {\rm Ri}_f \le 0.23$), and regime 3 (both Ri and Ri_f > 0.23). After harvest, in regime 1, stability varied from near-neutral to weakly stable and both MOST and HOST were applicable to estimate the momentum fluxes and $V_{\rm TKE}$ as a function of mean wind speed. In regime 2, the momentum flux deviated from the MOST linear relationship as stability increased. In regimes 1 and 2, a HOST-defined threshold wind speed V_s was identified beyond which $V_{\rm TKE}$ increased linearly with wind speed at a rate of 0.26 for all observation heights. Below this threshold wind speed, $V_{\rm TKE}$ behaved independent of mean wind and observation heights. Alternatively, for preharvest periods, MOST was applicable in regimes 1 and 2 for all heights and HOST was applicable with reduced V_s for heights above the crop layer. Regime 3 during pre- and postharvest consisted of strongly stable periods and very weak to weak winds, where MOST was found to be invalid and $V_{\rm TKE}$ remained low and independent of wind speed. The results suggest that roughness due to crops enhances the turbulence generation at lower wind speeds.

KEYWORDS: Turbulence; Boundary layer; Stability; Microscale processes/variability; Atmosphere-land interaction

1. Introduction

Although stable boundary layers (SBL) occur very frequently, understanding of the complexities of their evolution, the spatial and temporal structure of thermodynamic characteristics, and transfer of energy between the surface and lower atmosphere through turbulent processes lags those of neutral and unstable boundary layers (Mahrt 2014; LeMone et al. 2019; and others). Proper understanding of SBL processes and their accurate representation in numerical models is required to adequately characterize and simulate how atmosphere–surface interactions evolve during the considerable periods of time when there is a net downward flux of energy from the atmosphere to the surface (Mahrt 2014).

Indeed, the most commonly used classifications of stability within an SBL, ideally based on the strength of stratification, are either weakly or strongly stable. The division between weakly and strongly stable is based on its impact on wind speed profiles or reduction of the continuous vertical transport of energy to periods of intermittent turbulence (Mahrt et al. 2013; Mahrt 2014; Mahrt et al. 2015; Sun et al. 2016). To understand and properly define the stability regimes requires observations in a wide range of topographic conditions for long periods of time to obtain representative measurements. For example, as turbulence evolves from continuous daytime mixing processes to increasingly infrequent intermittent turbulent

Corresponding author: Sudheer R. Bhimireddy, sudheer@illinois.edu

eddies in the evening, there is an increased amount of measurement time needed to properly characterize rates of turbulent transfer (LeMone et al. 2019).

LeMone et al. (2019) point out that SBLs exhibit "smallerscale and weaker turbulence, greater sensitivity to terrain, and more heterogeneous structure." One of the most critical outstanding questions in simulating SBLs is whether parameterizations developed from observations in one environment will be adequate for conditions observed in others. Monin-Obukhov similarity theory (MOST) is widely used to model the near-surface turbulence statistics in the stratified atmospheric boundary layer (Monin and Obukhov 1954). Testing the validity of MOST during SBL conditions has been the subject of several studies (e.g., Mahrt 1998; Grachev et al. 2005; Optis et al. 2014; and Sun et al. 2016), and it is generally agreed that MOST does not apply in stable conditions. Field campaigns, like the Stable Atmospheric Boundary Layer Experiment in Spain 1998 (SABLES 98; Cuxart et al. 2000) and the 1999 Cooperative Atmosphere-Surface Exchange Study (CASES-99; Poulos et al. 2002), obtained measurements of turbulence quantities during SBL periods and produced valuable datasets that are being used to develop new similarity functions and parameterizations (Yagüe et al. 2006; Chenge and Brutsaert 2005). More recently, data from the Boundary Layer Late Afternoon and Sunset Turbulence (BLLAST) campaign (Lothon et al. 2014) allowed for testing of such relationships in the transition periods between buoyant turbulent forcing during the day to stable stratification as night progressed (Yus-Díez et al. 2019).

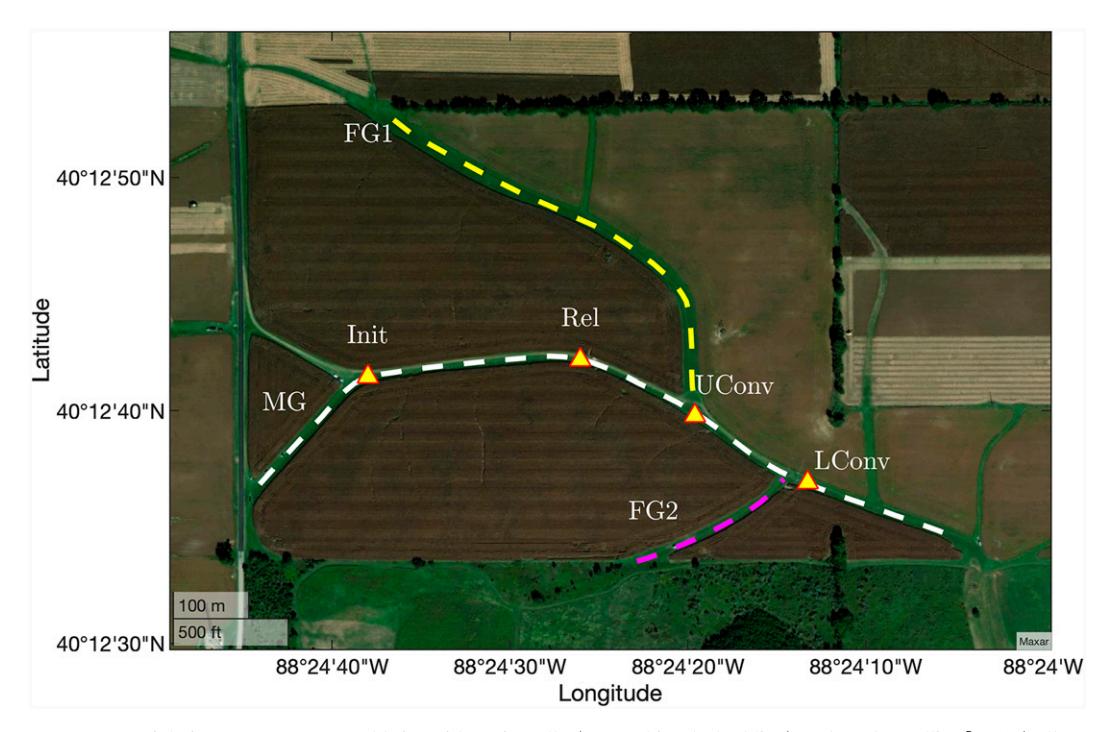


FIG. 1. Aerial view of SAVANT field site with main gully (MG; white dashed line) and feeder gullies [FG1 (yellow dashed line) and FG2 (magenta dashed line)]. Also shown are the ISFS sites corresponding to the initiation (Init), release (Rel), upper-convergence (UConv) and lower-convergence (LConv) towers. The Init and UConv towers are 10 m tall, and the Rel and LConv towers are 20 m tall. The data were generated from USDA Farm Service Agency maps using MATLAB.

Using the data collected over relatively flat grassland during the Microfronts project, Mahrt (1998) observed that MOST is valid for weakly stable SBL and becomes increasingly invalid as the stability increases. Similarly, Grachev et al. (2005) observed that MOST works well for weakly stable

regimes and its validity is improved by redefining the scaling variables in terms of local fluxes for transitional regimes over the Arctic pack ice. Using the data from a 60-m tower during CASES-99, Sun et al. (2016) observed that MOST bulk formulas in SBL are limited to a very thin layer (less than 10 m)

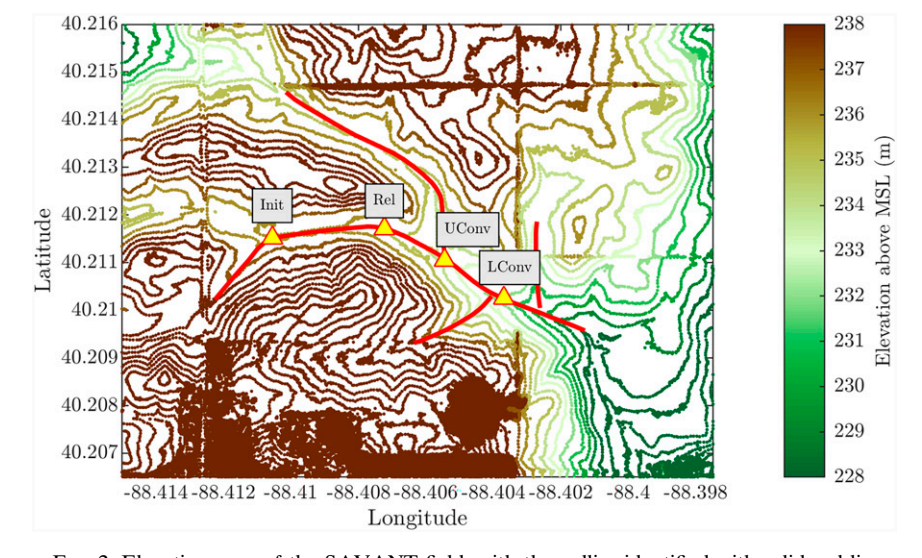


FIG. 2. Elevation map of the SAVANT field, with the gullies identified with solid red lines. The Init tower is located at 227 m MSL, and the UConv and LConv towers are at 222 and 220 m MSL, respectively. The towers are marked as yellow triangles.

TABLE 1. Drainage-flow detection criteria for observations up to 4.5 m above ground.

Variable observed	Range or threshold value
Wind speed	$< 2 \text{ m s}^{-1}$
Wind direction	$290^{\circ} \pm 10^{\circ}$
Friction velocity	$< 0.1 \text{ m s}^{-1}$
Surface heat flux	$-30 < H < 0 \text{ W m}^{-2}$
Wind direction profile	$ \partial \mathrm{UDir}/\partial z > 0.1^\circ \mathrm{m^{-1}}$
Temperature profile	$\partial \theta / \partial z > 0.2 \text{ K m}^{-1}$

near the surface. Optis et al. (2014) also concluded that MOST is accurate only at low levels and weakly stable periods from the observations collected using a 213-m tower. This was confirmed by Liang et al. (2014), who concluded that MOST is valid for weak winds and weakly stable conditions in a region of complex terrain. Such efforts raise the question of whether to replace or adjust MOST relationships in developing appropriate turbulent transfer parameterizations for SBL with very stable conditions, as well as identifying the specific stability conditions in which MOST no longer applies.

Sun et al. (2012, 2020) highlighted that MOST bulk formula performs reasonably well irrespective of wind speed for a special neutrality achieved when there is no surface heating or cooling taking place. To address the questions of turbulent processes in very stable conditions, using the observed relations between the turbulent variables (such as friction velocity) and the wind speed, Sun et al. (2012) formulated the hockey-stick transition (HOST) theory. HOST asserts that during stable conditions, a threshold wind speed could be identified below which the turbulence is generated entirely by local instabilities. Above the threshold wind speed, the turbulence magnitude varies with height and is generated by the bulk shear between the height and the surface (Sun et al. 2012, 2016, 2020). Sun et al. (2012) identified a third regime where surface generation of turbulence could not explain the greater turbulence magnitudes observed. In those cases, very large wind shear above the surface, usually associated with the low-level jet, resulted in downward fluxes of turbulent eddies and greater fluxes for low wind speeds than predicted by local instabilities alone (Sun et al. 2012).

The HOST theory was developed using the data from a 60-m tower over relatively flat terrain during CASES-99 (momentum roughness height during CASES-99 was estimated to be 0.027 m; Vickers and Mahrt 2004). Although MOST and HOST theories had been validated in multiple studies (Mahrt et al. 2013; Bonin et al. 2015; Yus-Díez et al. 2019), most of them were for relatively flat terrains with uniform and low roughness heights. A recent study by Yus-Díez et al. (2019) using BLLAST campaign data tested the effect of nearby orography on the HOST theory and found that the flows affected by the orographic features deviate from HOST. To our knowledge, the effect of local roughness due to presence of crops on the HOST theory has not been studied in the past. In this work, we address this by using the Stable Atmospheric Variability and Transport (SAVANT) campaign dataset taken in an area of corn and soybean crop (described below).

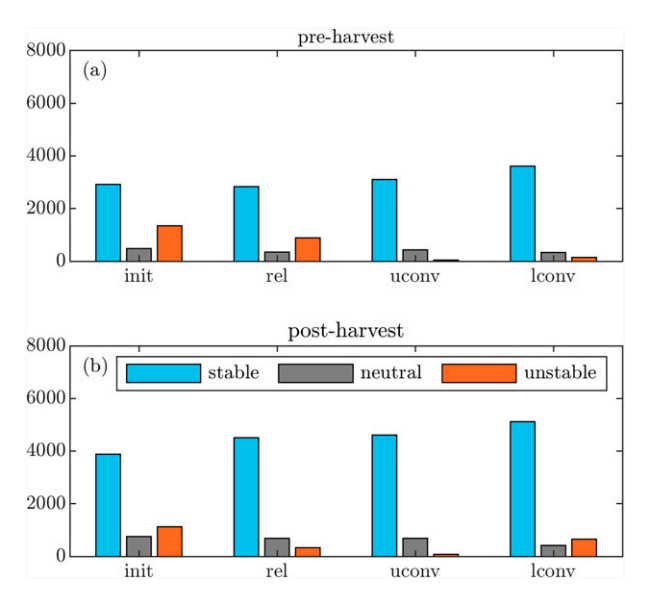


FIG. 3. Static stability regime frequency during nighttimes of all the (a) preharvest and (b) postharvest days during the campaign. Gray indicates neutral and near-neutral conditions, blue shows stable conditions, and orange indicates unstable conditions.

The current study seeks to augment the understanding of turbulent transfer in SBL conditions using observations taken during the SAVANT experiment in an area of shallow-slope topography, with a specific focus on the change in surface friction due to harvest of a deep corn crop (Hiscox et al. 2019, 2022, manuscript submitted to *Bull. Amer. Meteor. Soc.*). The objectives of the present study are

- to test MOST and HOST theories under stable conditions during pre- and postharvest of corn crop and
- to define turbulent regimes based on stability where MOST and HOST perform well.

Note that HOST is not intended to estimate the flux–gradient relationship like MOST. On the other hand, HOST explains the role of nonlocal eddies in turbulent mixing and their dependence on mean wind speed. The analysis presented in this study tests MOST and HOST theories individually and is not intended to conclude which one works better for SBL processes, rather this study focuses on the stability regimes and surface roughness effects on the applicability of MOST and HOST frameworks. The availability of data before and after a crop harvest adds novelty to our study. We can test the effect of surface roughness on the turbulence kinetic energy and its variation, and on the validity of the HOST and MOST relationships. In addition, we divided the data into different regimes based on Richardson numbers to better define conditions for which MOST and HOST theories are applicable.

The rest of the paper is structured as follows: section 2 details the site characteristics and the instrumentation used during SAVANT. Section 3 details the method followed to derive the variables used in the paper. Section 4 details the overall meteorological conditions and results of the MOST and HOST validity in terms of local stability and surface roughness. Section 5 gives the summary of the analysis presented.

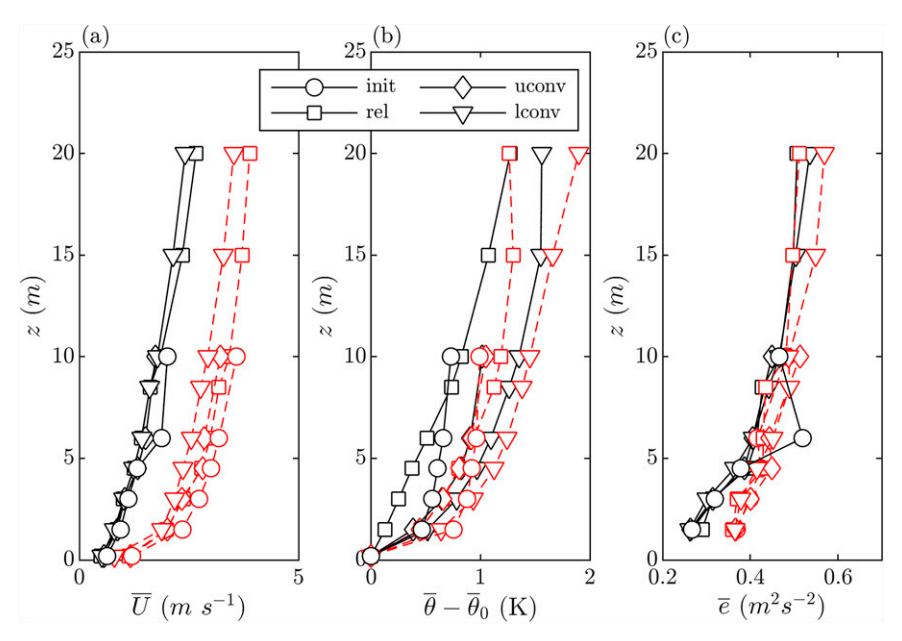


FIG. 4. Mean profiles of (a) wind speed, (b) potential temperature gradient, and (c) TKE during preharvest (black solid lines) and postharvest (red dashed lines) periods. The variables are height z, wind speed \overline{U} , potential temperature $\overline{\theta}$, potential temperature at 0.2 m $\overline{\theta}_0$, and turbulent kinetic energy \overline{e} .

2. Observations

a. Site characteristics

The SAVANT field campaign was conducted during September-November 2018, near Mahomet, Illinois. The campaign site was an agricultural field that has a shallow-slope topography. A schematic of the field site and gullies are given in Figs. 1 and 2. The field consists of one main gully and two feeder gullies. The main gully (MG) is 1040 m long and 8.91 m wide at the narrowest point, with an elevation difference of 10.66 m between the top and bottom. The feeder gully (FG1) is 592 m long and 15 m wide and a second feeder gully (FG2) is 226 m long and 8 m wide. The elevation differences along FG1 and FG2 are 4.88 and 4.57 m, respectively. During preharvest, the main gully has corn crop on either side until the point of intersection with FG1. Thereafter, corn is on the south and soy crop is on the north until the end of the gully. FG2 has corn crop on either side, and FG1 has corn on the south and soy crop on the north sides of the gully. There were no trees within 300 m of the initiation tower. The grass cover in the gully was around 25-30 cm tall, whereas the corn crop was approximately 3 m tall and the soy crop was approximately 0.9 m tall.

b. Instrumentation

During the SAVANT campaign, a dense array of instruments was deployed along the main gully on four Integrated Surface Flux System (ISFS) towers from the NCAR Earth Observing Laboratory's (EOL) Lower Atmospheric Observing Facilities. Tower locations are identified in Fig. 1. The 10-m-tall ISFS towers were named initiation (Init) tower and upper-convergence

(UConv) tower, and the 20-m-tall ISFS towers were named release (Rel) tower and lower-convergence (LConv) tower.

Data were collected from 15 September to 27 November 2018, and sensors collected data continuously unless interrupted by infrequent power failure or maintenance tasks. Campbell Scientific CSAT3A sonic anemometers were used to measure 3D wind components at 20 Hz. The theodolite measurements were used to apply correct directional rotations (NCAR/EOL In-Situ Sensing Facility 2021). Sonic anemometers were located at 1.5, 3, 4.5, 6, and 10 m above ground on all towers, and additional CSAT3A anemometers were located at 8.5, 15, and 20 m on the Rel and LConv towers. Gill WindObservers were deployed to measure 2D winds close to the surface (0.2 m AGL). Sensiron SHT75 Humidity and Temperature sensors were used to get the 20-Hz observations at 0.2, 1.5, 4.5, and 10 m on the Init and UConv towers and at 0.2, 1.5, 4.5, 8.5, 15, and 20 m on the Rel and LConv towers. CSAT EC-150 infrared absorption gas analyzers were used for H₂O and CO₂ measurements at 1.5 and 6 m on all towers, and additional EC-150 sensors were located at 20 m on the Rel and LConv towers. Solid-state barometers internal to the Campbell EC-150 H₂O/CO₂ analyzers were used to get pressure at 1.5 and 6 m on the Init tower. SAVANT data are available for download from the EOL website (https://doi. org/10.26023/NKWR-EYWS-5J0W).

3. Method

A temporal window of 5 min was used to obtain averaged statistics over equal time periods. The suitability of 5 min for time averaging was confirmed after identifying the gap scale from the multiresolution flux decomposition (MRFD) following the method of Vickers and Mahrt (2003). The gap scale of

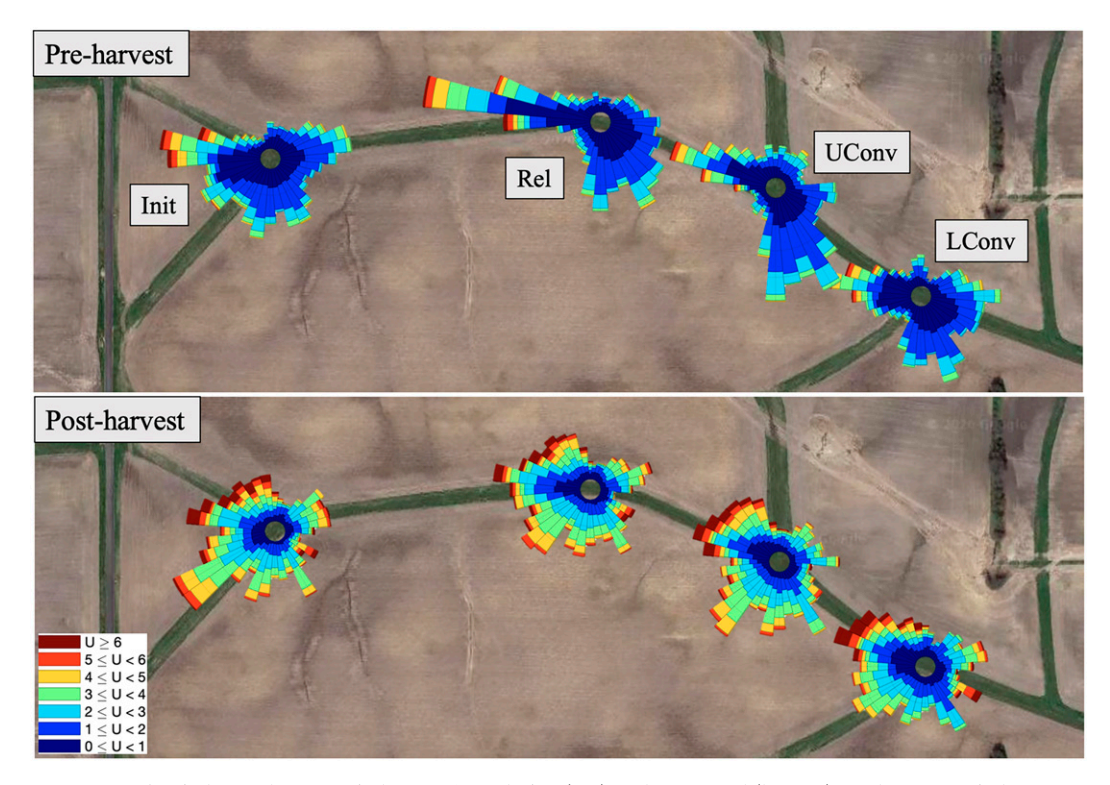


FIG. 5. Wind rose chart for winds up to 10 m during (top) preharvest and (bottom) postharvest periods.

5 min separates the turbulent fluxes that are related to the local conditions from mesoscale variations (Vickers and Mahrt 2003, 2006).

Following Sun et al. (2012), data from time periods during which nocturnal stable boundary layers are most common were kept, that is, data periods with negative near-surface sensible heat fluxes, no precipitation, and no significant mesoscale flow features were kept. For SBL observations, data from 1900 to 0700 central daylight time (CDT) were considered, which represents the approximate sunset and sunrise times during the SAVANT campaign. Note that local time is used throughout this article instead of UTC, since stable layers under consideration are highly related to local nightfall. The selection of this time window is based on the downward surface sensible heat flux measurements obtained near the towers. The data were further filtered to remove periods of down-gully cold-air drainage, as described below.

a. Derived variables

Several variables were derived using the 5-min-averaged values from each of the ISFS towers. From the absolute temperatures T measured by SHT75 sensors and barometric pressure P, the potential temperature was derived as $\theta = T(1000/P)^{0.286}$. Pressure values were linearly interpolated to the same heights as the temperature measurements. The static stability at each tower is then identified using the difference between θ at 0.2-and 10-m heights and classified as stable ($\Delta\theta > 0.1$), neutral ($-0.1 < \Delta\theta < 0.1$), and unstable ($\Delta\theta < -0.1$). For each 5-min-average period, the turbulent fluxes were estimated

using the eddy-correlation method. Using these fluxes, turbulent kinetic energy [TKE = $0.5(\overline{u'u'} + \overline{v'v'} + \overline{w'w'})$] and friction velocity [$u_* = (\overline{u'w'}^2 + \overline{v'w'}^2)^{0.25}$] were computed at heights where 3D sonic anemometers were present. Using TKE, a velocity scale $V_{\rm TKE} = {\rm TKE}^{0.5}$ (Sun et al. 2012) can be obtained to compare the HOST as reported by Sun et al. (2012, 2016). We examine the correlation of this velocity scale ($V_{\rm TKE}$) with bin-averaged wind speeds for pre- and postharvest periods. The TKE may contain nonturbulent components that can result in $V_{\rm TKE}$ having a finite value even as the wind speed approaches zero (Sun et al. 2012).

b. Detection of drainage flow

For the present analysis, we removed the 5-min data records that indicate the presence of a cold-type drainage flow. The occurrence of drainage flow was first identified from the aerosol lidar and Doppler lidar backscatter during the intensive observation periods (IOPs) and then corresponding tower data during those time periods was used to develop a criterion that can be applied to the non-IOP periods where lidar observations were absent. The criteria used to identify the drainage-flow time periods are listed in Table 1. The wind speed threshold of 2 m s⁻¹ and the wind direction threshold were tested for observations up to 4.5 m above ground. Wind speed and wind direction criteria listed in Table 1 are similar to the drainage-flow criteria during CASES-99 (Mahrt et al. 2001). While the 20° wind direction restriction might seem narrower, there exists no strong criteria of wind direction filtering for drainage flows in a similar gully topography. To be consistent, data from all four towers

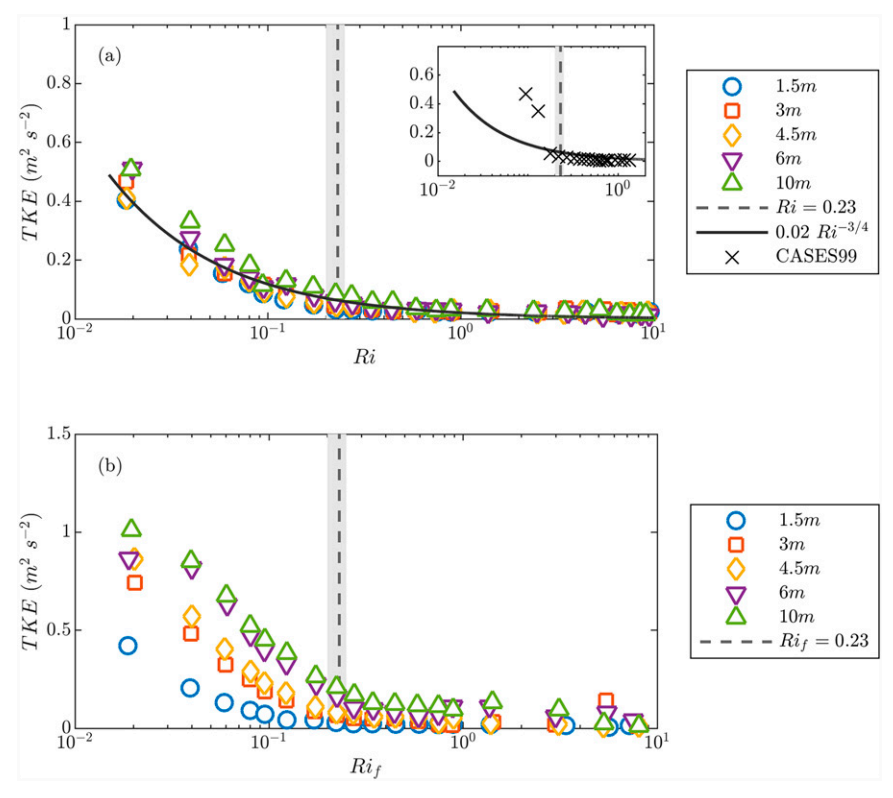


FIG. 6. Variation of bin-averaged postharvest night TKE for five levels on the Init tower with (a) gradient Richardson number Ri and (b) flux Richardson number Ri_f. The shaded region in (a) and (b) respectively corresponds to 0.2 < Ri < 0.25 and $0.2 < \text{Ri}_f < 0.25$, and the vertical dashed line represents Ri = 0.23 and Ri_f = 0.23, respectively. The solid black line in (a) represents a best-fit $0.02\text{Ri}^{-3/4}$ relation ($R^2 = 0.94$; significance level P < 0.001) between TKE and Ri.

were removed if drainage was observed at any tower or height. Approximately 18% of data points were excluded from analysis to remove the effect of drainage flow on the TKE statistics.

c. Monin-Obukhov similarity relations

MOST states that the near-surface turbulence variables are functions of a stability parameter ($\zeta = z/L$), where z is the measurement height and L is the Monin-Obukhov length scale obtained using

$$L = -\frac{u_*^3 \theta}{\kappa g \overline{w'} \theta'},\tag{1}$$

where κ is the von Kármán constant. The nondimensional shear from the mean wind speed was calculated from observations using

$$\phi_m = \frac{kz}{u_*} \frac{\partial U}{\partial z}.$$
 (2)

The widely used relation between ϕ_m and ζ is a linear one of the form

$$\phi_m = a + b\zeta,\tag{3}$$

where a (=1) and b (\approx 5) are constants obtained by fitting the observations from several field experiments under different

conditions (Businger et al. 1971; Dyer 1974; Garratt 1994; Wyngaard 2010). While the simple linear relation works reasonably well for most of the situations of SBL, especially for $\zeta < 1$, more complex forms are available in the literature. For example, Chenge and Brutsaert (2005) using the CASES-99 dataset found that the linear relationship between ϕ_m and ζ is valid up to $\zeta = 0.8$ and then levels off following

$$\phi_m(\zeta) = c + a \left[\frac{\zeta + \zeta^b (1 + \zeta^b)^{(1-b)/b}}{\zeta + (1 + \zeta^b)^{1/b}} \right],\tag{4}$$

with a = 6.1, b = 2.5 and c = 1. Grachev et al. (2007) developed functional forms for ϕ_m using data from the Surface Heat Budget of the Arctic Ocean (SHEBA) experiment, as

$$\phi_m(\zeta) = 1 + \frac{6.5\zeta(1+\zeta)^{1/3}}{1.3+\zeta}.$$
 (5)

Later Sorbjan and Grachev (2010) examined the ϕ_m forms using data from both SHEBA and CASES-99 and found that ϕ_m follows a linear form, $\phi_m(\zeta) = 1 + 4.7\zeta$, for "weakly stable" conditions with $\zeta < 0.6$ and follows a power-law form, $\phi_m(\zeta) = 5.187\zeta^{3/5}\zeta$, for "very stable" conditions with $\zeta > 0.6$. All expressions for nondimensional shear are examined in this study.

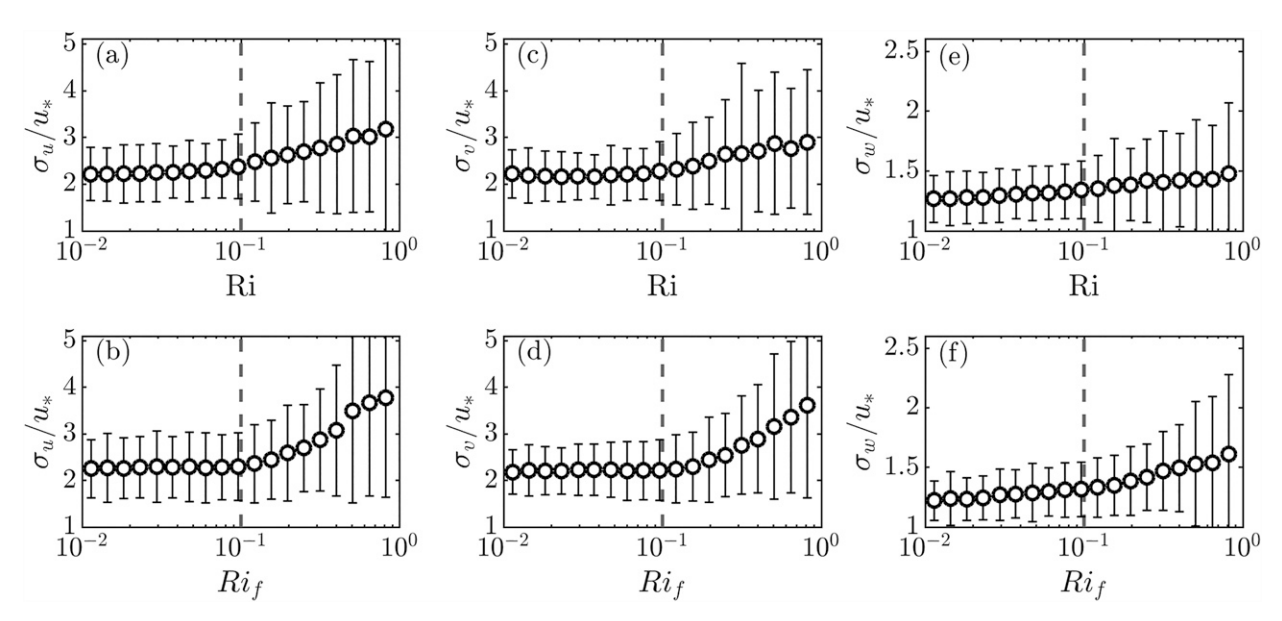


FIG. 7. Variation of bin-averaged velocity standard deviations scaled by the friction velocity with (top) Ri and (bottom) Ri_f at 4.5 m on the Init tower for postharvest nights, showing (a),(b) u-velocity standard deviation; (c),(d) v-velocity standard deviation; and (e),(f) vertical velocity standard deviation. The vertical dash line represents Ri = 0.1 (top panel) and $Ri_f = 0.1$ (bottom panel).

Grachev et al. (2013) tested the applicability of the MOST relationships [Eqs. (3) and (4)] based on the gradient Richardson number,

$$Ri = \left(\frac{g}{\theta}\right) \frac{\frac{d\theta}{dz}}{\left(\frac{dU}{dz}\right)^2},\tag{6}$$

and flux Richardson number,

$$\operatorname{Ri}_{f} = -\left(\frac{g}{\theta}\right) \frac{\overline{w'\theta'}}{u_{*}^{2} \left(\frac{dU}{dz}\right)}.$$
 (7)

Using data from SHEBA, they found that the MOST is applicable when Ri < 0.20–0.25 and Ri_f < 0.20–0.25 limitations are applied to filter the data. Grachev et al. (2013) showed that both Ri and Ri_f should be less than a critical value (0.2–0.25) for the local similarity theory to be applicable in the SBL and to ensure that the inertial subrange associated with the Richardson-Kolmogorov energy cascade exists. Liang et al. (2014) also used a critical Ri = 0.3 to filter the data so they follow MOST over complex topography. Howard (1961), using linear stability analysis for steady, two-dimensional flows, estimated that beyond a critical gradient Richardson number Ri of 0.25, turbulence completely decays. However, later field campaigns observed turbulence at very high Ri values (Ri > 100) and so the concept of a critical Richardson number is questionable and became a controversial issue. Unlike Ri, flux Richardson number Rif directly compares the buoyant destruction of turbulence with its shear production component. Freire et al. (2019) have used Ri_f to identify a critical value (Ri_f ≈ 0.21) beyond which turbulence cannot be sustained in a tall canopy (Fuentes

et al. 2016). This critical flux Richardson number value varies from 0.2 to 1.5 based on the surface properties such as surface roughness or heterogeneity (Grachev et al. 2013; Babić and Rotach 2018; Chamecki et al. 2018). We follow a similar approach to study the SAVANT data and define three regimes using both Ri and Ri_f (see section 4b) where the turbulence statistics (i) agree with MOST (regime 1), (ii) starts deviating from MOST (regime 2), and (iii) do not agree with MOST (regime 3).

4. Results and discussion

a. Overview of nighttime meteorological conditions during SAVANT

Figure 3 gives the number of stable, neutral, and unstable 5-min periods observed during 1900–0700 CDT for preharvest and postharvest days. After the filtering described above, a total of 16474 five-minute periods were available prior to harvest and 22 824 five-minute periods were available postharvest. The static stability was estimated to be stable 75% of the time, unstable 15% of the time, and neutral 10% of the time for preharvest periods, with only a slight increase in percentage of stable conditions (to 80%) postharvest. For this study, only data with $\Delta\theta > 0$ (stable and neutral) were considered.

Even though the distribution of stability values changed little after harvest, the wind speed and potential temperature profiles changed considerably. After harvesting of the crop, the mean wind speed at all heights approximately doubled (Fig. 4a), and the mean wind shear in the lower 10 m increased from 0.14 to 0.23 s⁻¹. The mean potential temperature dropped by 12 K postharvest, which could be the result of seasonal change in the Midwest. Although the temperature dropped by such a large extent, the vertical gradient of

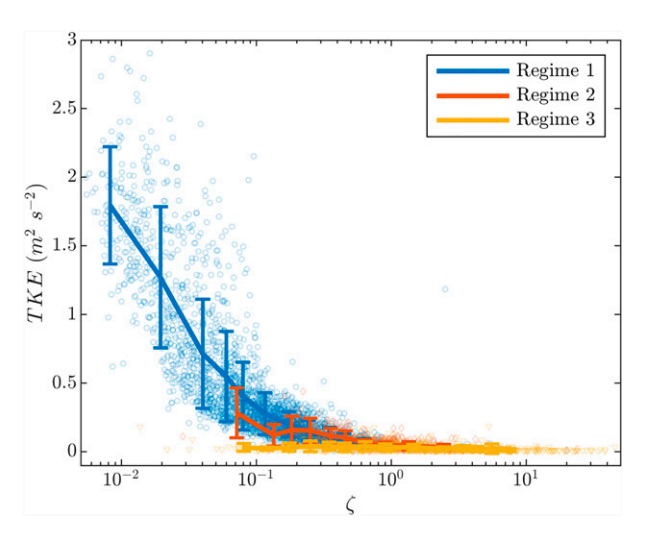


FIG. 8. Variation of bin-averaged TKE plotted against the Monin–Obukhov stability parameter ζ at 4.5 m on the Init tower for all nights. Shown are regime 1 (0 < Ri \leq 0.1 and 0 < Ri_f \leq 0.1), regime 2 (0.1 < Ri \leq 0.23 and 0.1 < Ri_f \leq 0.23), and regime 3 (Ri > 0.23 and Ri_f > 0.23).

potential temperature (Fig. 4b) remained approximately the same. Figure 4c gives the vertical profiles of TKE for pre- and postharvest periods. A significant jump in the TKE could be seen at 6 m on the Init tower, similar variation is observed for mean winds as well. We hypothesize this as the result of an internal momentum boundary layer that developed above the corn crop surrounding the Init tower for preharvest periods. Another important change during postharvest was in the wind direction up to and including 10 m above the ground. Figure 5 shows the wind-rose plot for the winds up to and including 10 m at all four towers during preharvest and postharvest periods. Prior to the crop harvest dominant winds were approximately aligned with the gully. While some influences of changing synoptic conditions are likely, the abrupt changes in low-level wind characteristics suggests a channeling effect by the crops. The postharvest winds were more widely distributed, suggesting limited channeling.

b. Critical Richardson number for SAVANT observations

This study uses the turbulent kinetic energy observations from the initiation tower during postharvest nights during SAVANT to identify the critical values for both Ri and Ri_f. Figure 6 gives the variation of bin-averaged TKE with Ri and Ri_f at five different levels on the Init tower for postharvest nights. At each observation height, after Ri and Ri_f exceed the range 0.2–0.25, the bin-averaged TKE reduced sharply and remained less than 5% of its maximum value. By taking the average of cutoff Ri and Ri_f for 1.5–10 m, we use Ri \approx Ri_f \approx 0.23 as the critical value for the rest of the analyses. Similar decay of bin-averaged TKE up to Ri range of 0.2–0.25 was observed (shown in inset plot of Fig. 6a) for stable nights during CASES-99 (Banta et al. 2007). For Ri, TKE varied with a best fit of 0.02Ri $^{-3/4}$ regardless of observation height (Fig. 6a). However, for Ri₆ TKE decreased at different rates with height, with

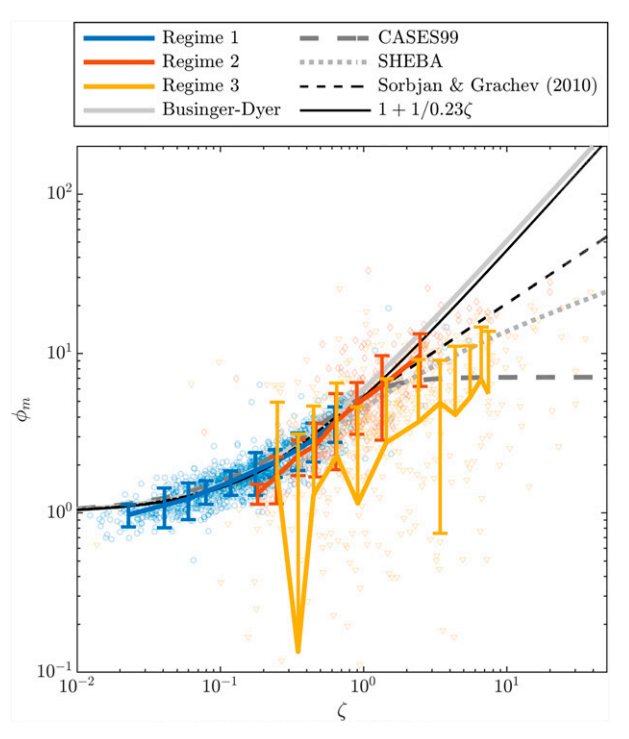


FIG. 9. Variation of bin-averaged ϕ_m with ζ at 4.5 m on the Init tower for postharvest nights. The thick solid gray line represents a Businger–Dyer relationship [Eq. (3) with a=1 and b=5], and the thick gray dashed line represents a fit using CASES-99 data [Eq. (4)] (Chenge and Brutsaert 2005). The thick gray dotted line represents a SHEBA function (Grachev et al. (2007). The black dashed line represents functional forms from Sorbjan and Grachev (2010) [their Eqs. (26a) and (27a)]. The solid black line represents Eq. (3) with a=1 and b=1/0.23.

maximum TKE observed at 10 m (Fig. 6b). Grachev et al. (2013) observed similar trends for bin-averaged momentum fluxes versus Ri and Ri_f for stable nights during the SHEBA experiment.

Based on Fig. 6, we define a regime for all the time periods when Ri and Rif were larger than 0.23 and the TKE stayed minimum. This regime where Ri and $Ri_f > 0.23$ is often considered as strongly stable regime of SBL. Sorbjan (2010) using the SHEBA data observed that the vertical velocity variance scaled by the TKE reaches a maximum around Ri = 0.1 and decreases further as Ri increases. Similar trend was observed for scaled vertical velocity variance for SAVANT initiation tower data (not shown) at $Ri = Ri_f \approx 0.1$, and it decreased as Ri and Ri_f increased. Figures 7a and 7b shows the variation of bin-averaged u-velocity standard deviation σ_u scaled by the friction velocity u* with Ri and Rif. The data suggest that σ_u/u_* is constant up to Ri = Ri_f ≈ 0.1 and increases as Ri and Ri_f increase. This constant value is found to be 2.25. Similar behavior was found for the scaled v-velocity standard deviation σ_{ν}/u_* (Figs. 7c,d) and the scaled vertical velocity standard deviation σ_w/u_* (Figs. 7e,f). Pahlow et al. (2001) observed similar trends for the scaled velocity standard deviations but against the stability parameter ζ based on the data from five distinct experiments (see their Table 1). Pahlow et al. (2001)

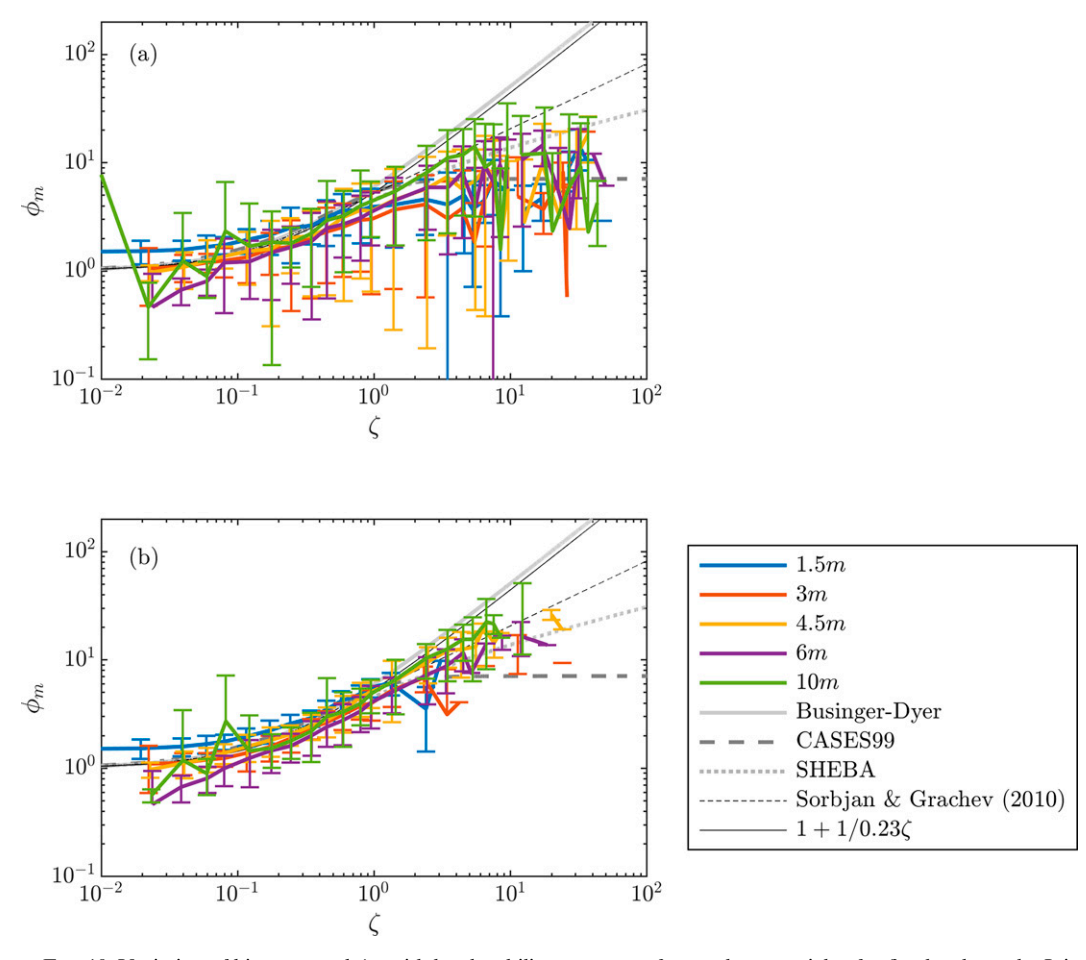


FIG. 10. Variation of bin-averaged ϕ_m with local stability parameter for postharvest nights for five levels on the Init tower (a) without imposing any Ri restrictions on the data and (b) filtering out data points when Ri > Ri_{cr} = 0.23 and Ri_f > Ri_{cr} = 0.23.

argued that the increased scaled velocity standard deviations is due to dampening of turbulent motions for strongly stable stratification, and MOST becomes inapplicable as the size of turbulent eddies depends on the stability rather than the height above the surface. Note that u_* is a common variable for the scaled velocity standard deviations and Ris, and so the trend obtained in Figs. 7b, 7d, and 7f could be affected by selfcorrelation (Klipp and Mahrt 2004; Anderson 2009). Following Sorbjan (2010) and the behavior of scaled velocity standard deviations, we use $Ri = Ri_f \approx 0.1$ as another limiting value. The regime where $0.1 < Ri \le 0.23$ and $0.1 < Ri_f \le 0.23$ is comparable to the transition regime from weakly stable to strongly stable conditions as observed from the SHEBA experiment (Sorbjan 2010). The Ri threshold values considered to categorize the above regimes are comparable to those used by Liang et al. (2014).

c. Turbulent velocity scale profile for postharvest periods

To better understand the effect of stability on the TKE growth, another stability defining metric ζ was used. Figure 8 gives the variation of TKE with the Monin–Obukhov stability

parameter ζ for data collected at 4.5 m on the Init tower, which is at the top of the gully ("Init" in Fig. 1). Data at other heights have a similar pattern and so were excluded from Fig. 8. The data were categorized on the basis of the Ri and Ri_f limits. For the $0 < \text{Ri} \le 0.1$ and $0 < \text{Ri}_f \le 0.1$ regime, the TKE magnitude maximized in the weakly stable regime with $\zeta < 0.7$. For the $0.1 < \text{Ri} \le 0.23$ and $0.1 < \text{Ri}_f \le 0.23$ regime, the TKE magnitude decreased as the stability changed from weak to strong, that is, $0.5 < \zeta < 1.3$. For the Ri and Ri_f > 0.23 regime, the TKE was at its minimum, with an average value of $0.06 \text{ m}^2 \text{ s}^{-2}$, and did not vary with stability.

For upper convergence and lower convergence towers, higher turbulence magnitudes were observed for both Ri and $\mathrm{Ri}_f > 0.23$ during weakly stable conditions ($\zeta < 0.5$). The difference of TKE between the initial/release towers and the upper/lower convergence towers could be due to their location in the gulley. The initial and release towers were at the top of the gully and were thought to be affected more by background (mesoscale or larger) flows, whereas the lower and upper convergence towers were at the bottom of the gully and would be expected to have a greater influence from in-gully flow.

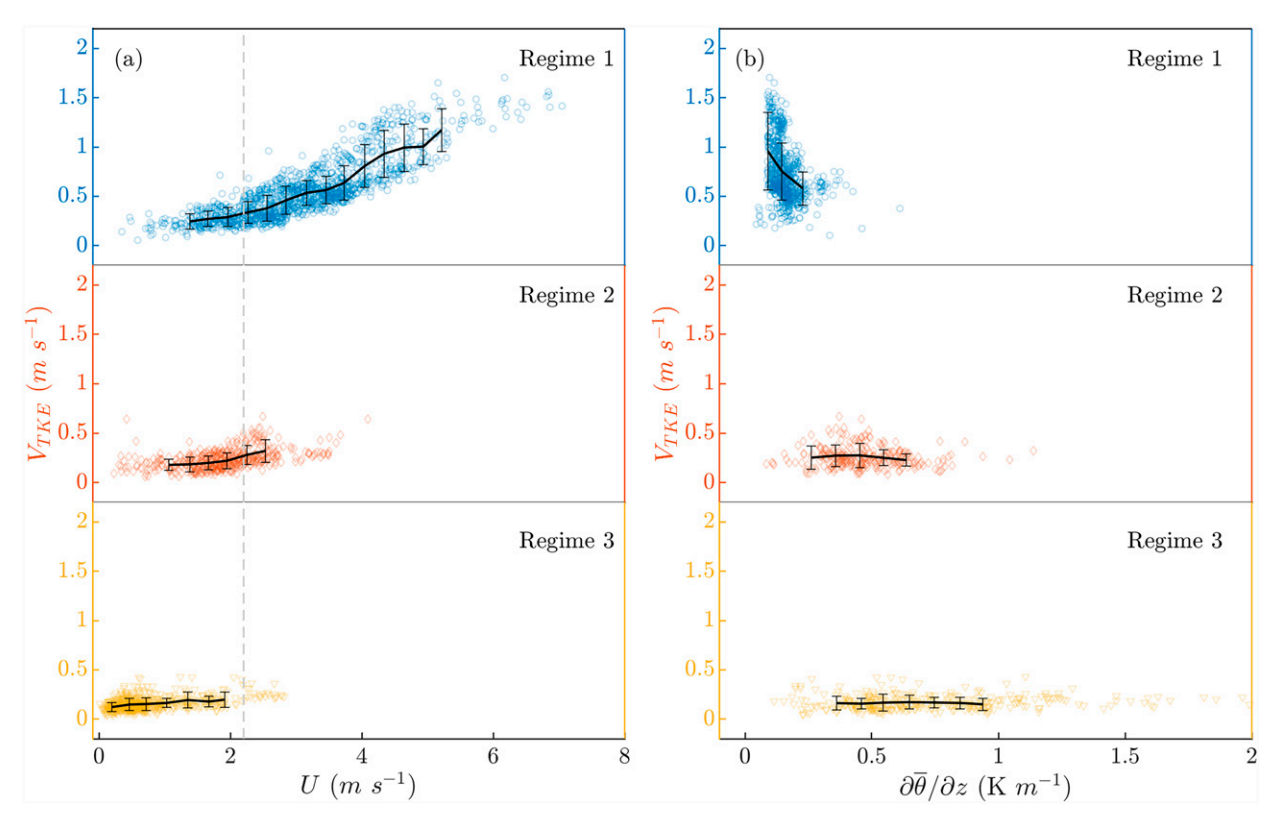


FIG. 11. Variation of $V_{\rm TKE}$ with (a) wind speed observed at 4.5 m and (b) potential temperature gradient between 4.5 and 0.2 m for postharvest nights classified into regimes on the basis of Ri and Ri_f criteria. The vertical dashed line in (a) represents the threshold wind speed at 4.5 m. Bins with fewer than 20 observations were not included in estimating the mean and standard deviation.

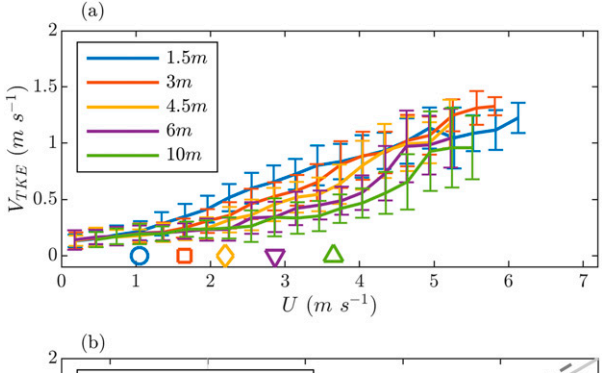
Next, to test the data against MOST relations, we study the variation of ϕ_m with stability parameter as shown in Fig. 9. The data with $0 < Ri \le 0.1$ and $0 < Ri_f \le 0.1$ criteria (regime 1) agreed well with the widely used Businger-Dyer relationship. Also, the standard deviation of ϕ_m observed in the 0.1 < Ri \leq 0.23 and $0.1 < Ri_f \le 0.23$ regime, 1.56, was more than (almost 3 times) the standard deviation in the $0 < Ri \le 0.1$ and $0 < Ri_f \le 0.1$ regime, 0.45. The standard deviation of ϕ_m is highest (4.55) in the Ri > 0.23 and $Ri_f > 0.23$ regime. The ϕ_m varied largely when $\zeta > 1$. From Fig. 9, the data in regime 3 do not follow the MOST relationship. For comparison, the relationship between ϕ_m and ζ obtained by Chenge and Brutsaert (2005) from CASES-99 data was also plotted in Fig. 9. As mentioned in Chenge and Brutsaert (2005), the levelling of ϕ_m for $\zeta > 1$ in CASES-99 is due to the presence of turbulence nonstationarity under strong stable conditions during CASES-99, which is not the case for our dataset [Following Liang et al. (2014), the turbulence nonstationary motions were not found in our dataset by comparing the 60-min-averaged TKE values with the 5-min averages]. No leveling off of ϕ_m for $\zeta > 1$ was observed for 5-min-averaged observations at the Init tower during SAVANT.

Figure 10 gives the variation of bin-averaged ϕ_m at different heights at the Init tower. For the entire dataset without imposing any Ri and Ri_f restrictions, the bin-averaged ϕ_m values seem to follow the MOST similarity relations for $\zeta \leq 0.1$

(except for observations at 10 m) and deviate thereafter, albeit with the data having very high standard deviations. The deviation from the similarity relations and the high standard deviation increased with increasing stability, also observed from SHEBA dataset (Grachev et al. 2013). After imposing Ri and Rif restrictions, data from regimes 1 and 2 were combined for simplicity, and their combined bin-averaged ϕ_m (Fig. 10b) was observed to follow the MOST similarity and to agree with the findings from SHEBA dataset (Grachev et al. 2013). Also, the data from the present study matched closely with the analytical forms given by Sorbjan and Grachev (2010) using data from SHEBA and CASES-99 and Eq. (5). The relationship between the dimensionless shear ϕ_m and ζ is influenced by the possible self-correlation because u_* exists as a common variable in estimating ϕ_m and ζ . Previous studies (Baas et al. 2006; Klipp and Mahrt 2004; Anderson 2009) highlighted that the effect of selfcorrelation becomes significant for stronger stability conditions. Baas et al. (2006) developed an alternative way of plotting ϕ_m against ζ independent from self-correlation, in which they use the linear relationship [Eq. (3), with a = 1] and study the variation of $u_*^2 dU/dz - u_*^3/(\kappa z)$ versus $(-g/\theta) \overline{w'\theta'}$, whose slope provides an estimate of the slope b in Eq. (3). This approach is limited because the linear relationship breaks down beyond ζ value of 1.5. We tested the SAVANT Init tower data for postharvest periods to estimate the slope by following Baas et al. (2006) and found it to be 4.15 (correlation coefficient squared $R^2 = 0.74$), which matches closely with the value of 4.35, plotted as a dark solid line in Fig. 8.

To understand the stable boundary layer conditions that favor the enhancement of TKE, we studied the variation of $V_{\rm TKE}$ with respect to the mean wind speed U. Sun et al. (2012) defined a threshold wind speed V_s below which V_{TKE} stays independent of mean wind speed, and, for wind speeds that are greater than V_s , V_{TKE} increases linearly at a rate of 0.25. Figure 11a illustrates the variation of 5-min-averaged V_{TKE} with wind speed at 4.5 m on the Init tower after harvest, separated into the three regimes. For the trends, V_{TKE} remained approximately constant below a wind speed of 2.20 m s⁻¹ for regimes 1 and 2. Beyond this wind speed value, as represented by vertical dashed lines in Fig. 11a, V_{TKE} increased linearly with wind speed, making $V_s = 2.20 \text{ m s}^{-1}$ for 4.5 m at the Init tower. No such threshold values were observed for regime 3. The spread of V_{TKE} in each of the regimes with respect to local potential temperature gradient between 4.5 and 0.2 m on the Init tower is shown in Fig. 11b. In regime 1, the bin-averaged $V_{\rm TKE}$ decreased with increasing stability (Fig. 11b). In regimes 2 and 3, while the overall bin-averaged and individual $V_{\rm TKE}$ values did not appear to depend on the local stability, their variation was greater in regime 2 than in regime 3 as seen from the error bars in Fig. 11b.

The variation of bin-averaged V_{TKE} with wind speed at all the observation levels after harvest is shown in Fig. 12a. As in Fig. 11a, V_{TKE} varied linearly with wind speed beyond a threshold value, and this threshold value increased with the observation height. We followed a similar approach as in Sun et al. (2012) in identifying the threshold wind speed, that is, at V_s the slope with which V_{TKE} varies with respect to U changes. For SAVANT data at the Init tower, the threshold wind speed values at each observation height were identified as 1.05 m s⁻¹ $(z = 1.5 \text{ m}), 1.65 \text{ m s}^{-1} (z = 3 \text{ m}), 2.20 \text{ m s}^{-1} (z = 4.5 \text{ m}),$ 2.87 m s⁻¹ (z = 6 m), and 3.65 m s⁻¹ (z = 10 m). The linear increase of $V_{\rm TKE}$ with U had a slope of approximately 0.26 as shown in Fig. 12b. This linear trend was also observed for CASES-99 data, which led to the HOST theory (Sun et al. 2012). For CASES-99, the linear increase of $V_{\rm TKE}$ had an observed slope of 0.25 and the threshold wind speed values increased with height. The deviation of a linear trend for 1.5 m in Fig. 12b is due to fewer observations with wind speeds stronger than 5 m s^{-1} at that level. For 1.5 m on the initiation tower, the number of observations with wind speed less than and including 5 m s⁻¹ is 4339, whereas it is 121 for winds stronger than 5 m s⁻¹. The threshold wind speed values observed during SAVANT were comparable to those observed during CASES-99. A significant difference between CASES-99 and SAVANT data at the Init tower is the absence of events where turbulence was interpreted to have originated at greater altitudes and intermittently coupled to the surface, observed as downward bursts of turbulence as reported in Sun et al. (2012). A downward transport of turbulence could be characterized by a decrease in wind speed and increased vertical velocity variance with height (Blumen et al. 2001; Mahrt and Vickers 2002; Sun et al. 2012). Using the time series variation of TKE, vertical velocity, and vertical velocity variance, the elevated turbulence and its possible downward



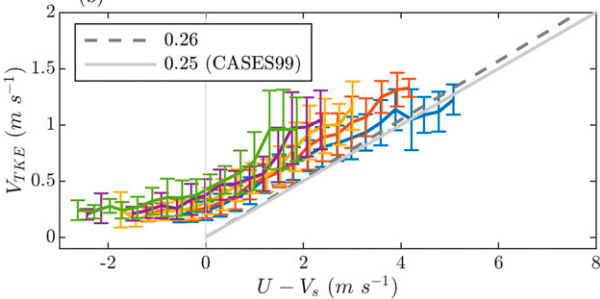


FIG. 12. (a) Profile variation of bin-averaged $V_{\rm TKE}$ with wind speed at the Init tower for data after the crop harvest and Ri and ${\rm Ri}_f > 0$ and Ri and ${\rm Ri}_f \le {\rm Ri}_{\rm cr} = 0.23$ criteria applied; (b) $V_{\rm TKE}$ as a function of "wind speed — V_s (threshold wind speed)" at five levels on the Init tower. Bins with fewer than 20 samples were excluded.

transport could not be identified at the Init tower during SAVANT.

d. Turbulent velocity scale profile during preharvest

To quantify the effect of crop roughness on the observed turbulence statistics, we estimated the roughness length using the flux method as outlined in Sun (1999). We give the summary of this method here. For detailed description, see Sun (1999). The flux method uses the momentum bulk formula from MOST such that the friction velocity is related to the mean wind speed through the roughness and stability parameters (Garratt 1994),

$$\ln\left(\frac{z-d}{z_0}\right) = \frac{U\kappa}{u_*} + \psi_m\left(\frac{z-d}{L}\right), \tag{8}$$

where z_0 is the roughness height, κ (=0.41) is the von Kármán constant, d is the displacement height, and ψ_m is the integral form of stability function ϕ_m that depends on ζ . For estimating the displacement height, the momentum bulk formula at two different heights was used during neutral conditions because $\psi_m = 0$ and z_0 could be eliminated through simple subtraction. As such, 30-min time averages were estimated and later averaged for all preharvest days to get the diurnal variations. We used these averaged quantities at 4.5 and 10 m on the Init tower during neutral conditions ($\Delta\theta \sim 0$) and estimated the displacement height d at the Init tower to be 1.7 m. By obtaining the displacement height, the only unknown left in the

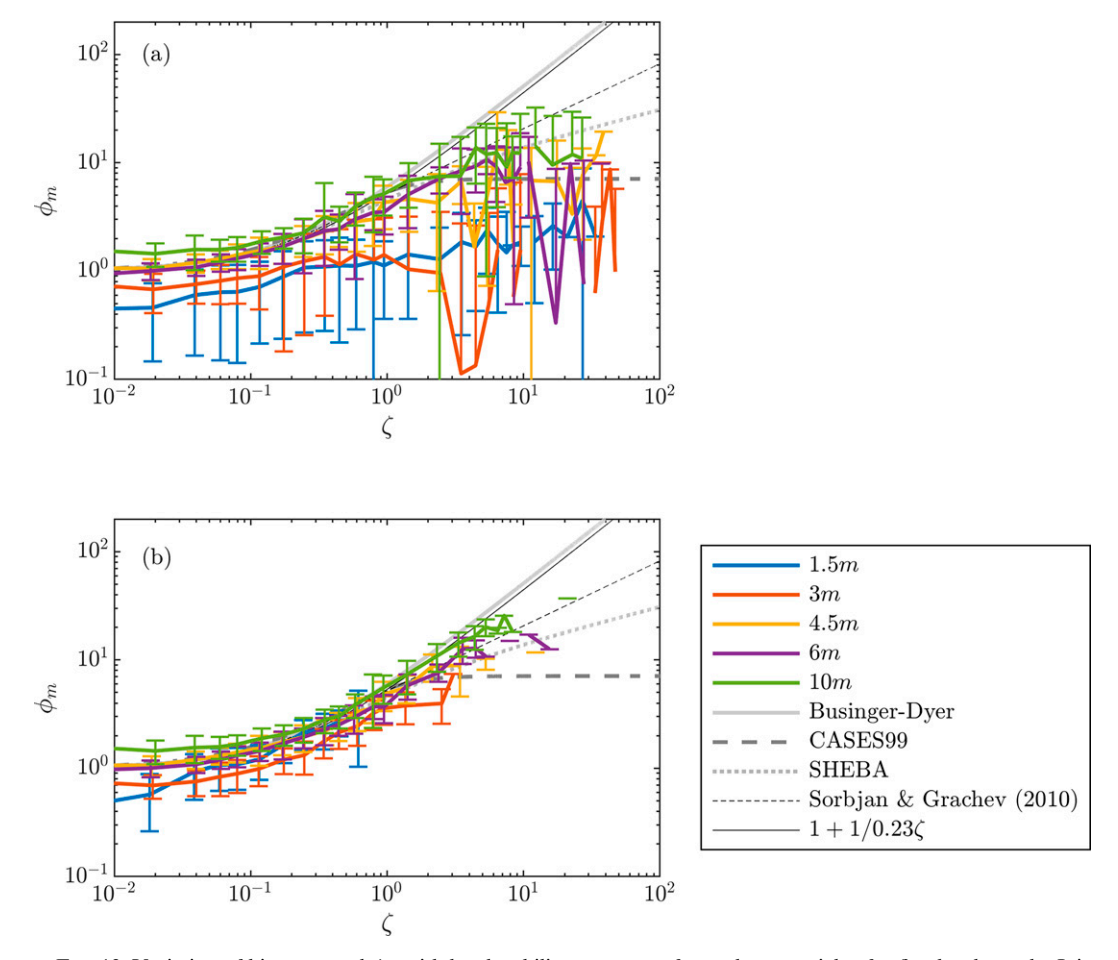


FIG. 13. Variation of bin-averaged ϕ_m with local stability parameter for preharvest nights for five levels on the Init tower (a) without imposing any Ri restrictions on the data and (b) filtering out data points when Ri > Ri_{cr} = 0.23 and Ri_f > Ri_{cr} = 0.23.

momentum bulk formula [Eq. (8)] is z_0 . Using fluxes and mean observations at all observation levels, the average roughness height estimated near the initiation tower is 0.41 m. As expected, the wind speed profile averaged for all of the preharvest nights at the Init tower was found to have different slope for heights 1.5–4.5 m when compared with the slope for observations above 6 m (Fig. 4a). The observations at 1.5 and 3 m were below the crop layer and were most affected. Note that the observations at 6 and 10 m might still be affected by roughness sublayer formed as a result of the crop underneath (Cionco 1972). Similarly, using Eq. (8), the roughness height during postharvest period is estimated as 0.05 m.

Prior to the crop harvest, at 4.5 m, higher turbulence was observed at lower wind speeds. This was observed at other tower locations as well (not shown), but the difference between the turbulence at 10 m before and after the harvest was highest at the Init tower. We hypothesize this is primarily due to the Init tower being surrounded by corn crop, whereas other towers have corn crop to the south and soybean crop to the north. Also, other towers are located along the gully where the slope changed gradually. These lead to different

roughness heights at towers (except the Init tower) that depends on the wind direction. Further, wind direction analysis revealed that the higher turbulence observed at lower wind speeds during preharvest occurred when the winds are from west-northwest (W-NW) or aligned along the gully. From the wind rose chart for winds up to 10 m, the predominant wind direction during preharvest is from W-NW (Fig. 5). The relief within a 1-km radius from the Init tower was about 20 m with elevated hills located toward west and north of the Init tower. In addition to the presence of hills, the crop line starts within 100 m west of the Init tower; this makes the estimation of a single roughness height based on the crop difficult.

In the presence of roughness elements, the variation of binaveraged ϕ_m at different heights (other than 1.5 and 3 m) at the Init tower, without imposing any Ri and Ri_f restrictions, followed the MOST similarity relations for $\zeta \leq 0.5$ (Fig. 13a) (similar to the trend observed for postharvest periods; Fig. 10a). Because the observations at 1.5 and 3 m were most affected by the presence of the crop layer, their ϕ_m variation deviated from the rest of the observations. After imposing Ri and Ri_f limits, however, observations at all heights followed the

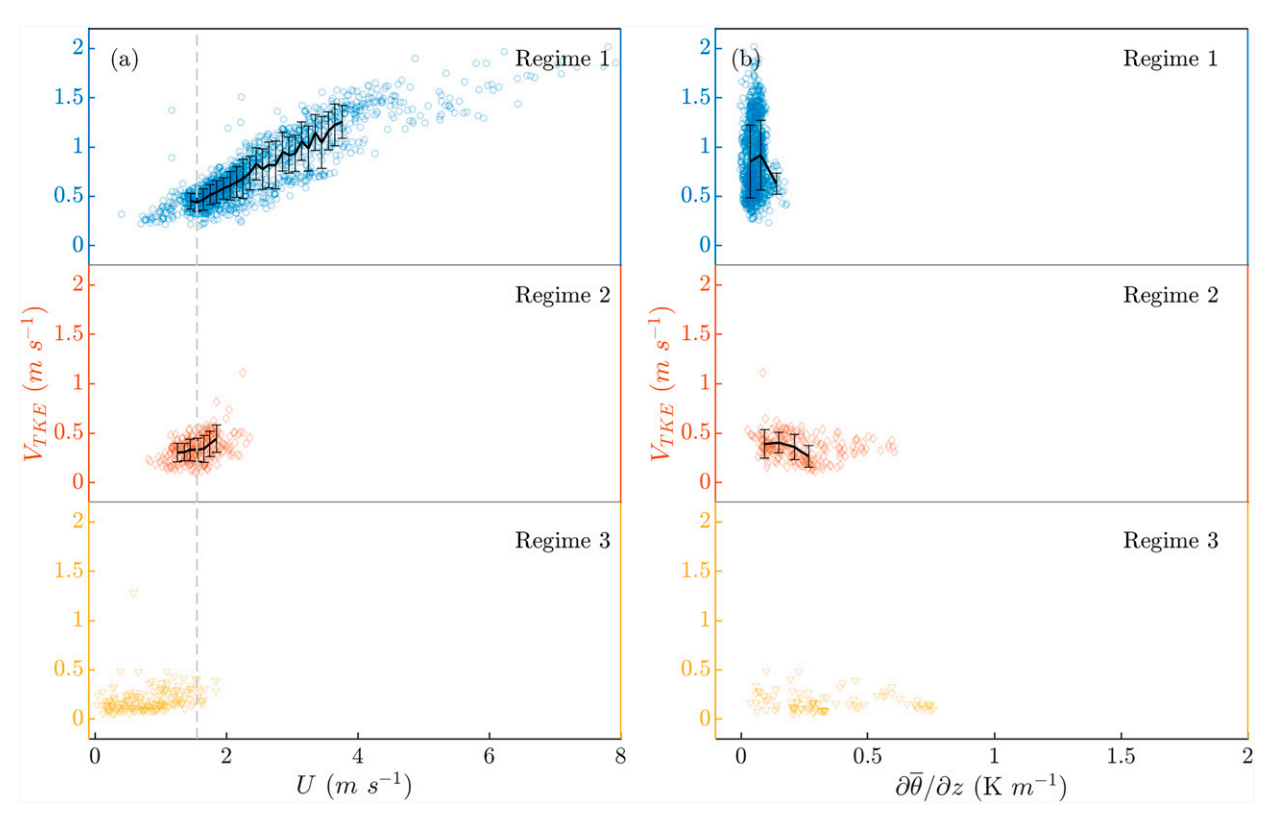


FIG. 14. Variation of $V_{\rm TKE}$ with (a) wind speed observed at 10 m and (b) potential temperature gradient between 10 and 0.2 m for preharvest nights classified into regimes on the basis of Ri and Ri_f criteria. The vertical dashed line in (a) represents the threshold wind speed at 10 m. Bins with fewer than 20 observations were not included in estimating the mean and standard deviation.

MOST relation trend (Fig. 13b) and agreed with the findings from SHEBA dataset (Grachev et al. 2013) like postharvest observations. Fig. 14a gives the variation of at 10 m for preharvest periods. Because the observed wind speeds during preharvest periods were weaker, finer wind speed bins had to be used to identify the threshold wind speeds. The V_{TKE} is approximately constant below a wind speed of 1.45 m s⁻¹ for regimes 1 and 2. Beyond this wind speed value, as represented by vertical dashed lines in Fig. 14a, V_{TKE} increases linearly with wind speed, making $V_s = 1.45 \text{ m s}^{-1}$ for 10 m at the Init tower for preharvest. Similar to the postharvest observations, the bin-averaged V_{TKE} at 10 m decreased with increasing stability (Fig. 14b). In regimes 2 and 3, although the overall $V_{\rm TKE}$ values did not depend on the local stability, their variation was greater in regime 2 than in regime 3, again matching the trend observed for postharvest observations. Similar to postharvest periods, the variation of ϕ_m with ζ matched closely the analytical form given by Sorbjan and Grachev (2010) and agrees well with Eq. (5).

Unlike ϕ_m trends similar to the postharvest observations, the variation of bin-averaged $V_{\rm TKE}$ with mean wind speed (Fig. 15) does not match the observed trends as in Fig. 12a. High TKE values ($\approx 0.5~{\rm m}^2~{\rm s}^{-2}$) were observed close to the surface at low wind speeds ($U < 1.5~{\rm m~s}^{-1}$), and no threshold wind speed were observed for $z \leq 3~{\rm m}$. Obviously, the difference may be caused by the roughness change before and after harvest. The bin-averaged $V_{\rm TKE}$ at all heights on the Init

tower varied with mean wind speed with a slope of 0.245. Although HOST relations for complex terrain were studied in the past, such as during the BLLAST campaign (Yus-Díez et al. 2019), the conditions present during SAVANT were unique and represent a first-of-a-kind complexity in terms of crop and terrain relief. The presence of higher TKE values at wind speeds less than 1.5 m s⁻¹ should not be treated as a result of top-down turbulence events as reported in Sun et al. (2012) or Yus-Díez et al. (2019). We hypothesize that an additional momentum boundary layer forms because of the presence of a crop layer ~100 m west (upwind) of the Init tower and that this boundary layer may be responsible for higher turbulence observed at the lower wind speeds. Further analysis is needed to test this hypothesis, and such work would be beyond the scope of this study. For z > 3 m, the bin-averaged $V_{\rm TKE}$ profiles versus U showed a subtle variation in slope when finer bin widths were used. This can be seen from the zoomed-in plots of $V_{\rm TKE}$ versus U in Fig. 15. The threshold wind speed values identified for preharvest periods were: 0.55 m s⁻¹ (z = 4.5 m), 0.85 m s⁻¹ (z = 6 m), and 1.45 m s⁻¹ (z = 10 m). Increased roughness length reduces the threshold wind speed (Mahrt et al. 2013). From the present dataset, the threshold wind speed reduced from 2.20 to 0.55 m s⁻¹ at z = 4.5 m for the higher roughness length. Figure 16 compares the threshold wind speed profiles for pre- and postharvest data for SAVANT. Also, data from other field campaigns were

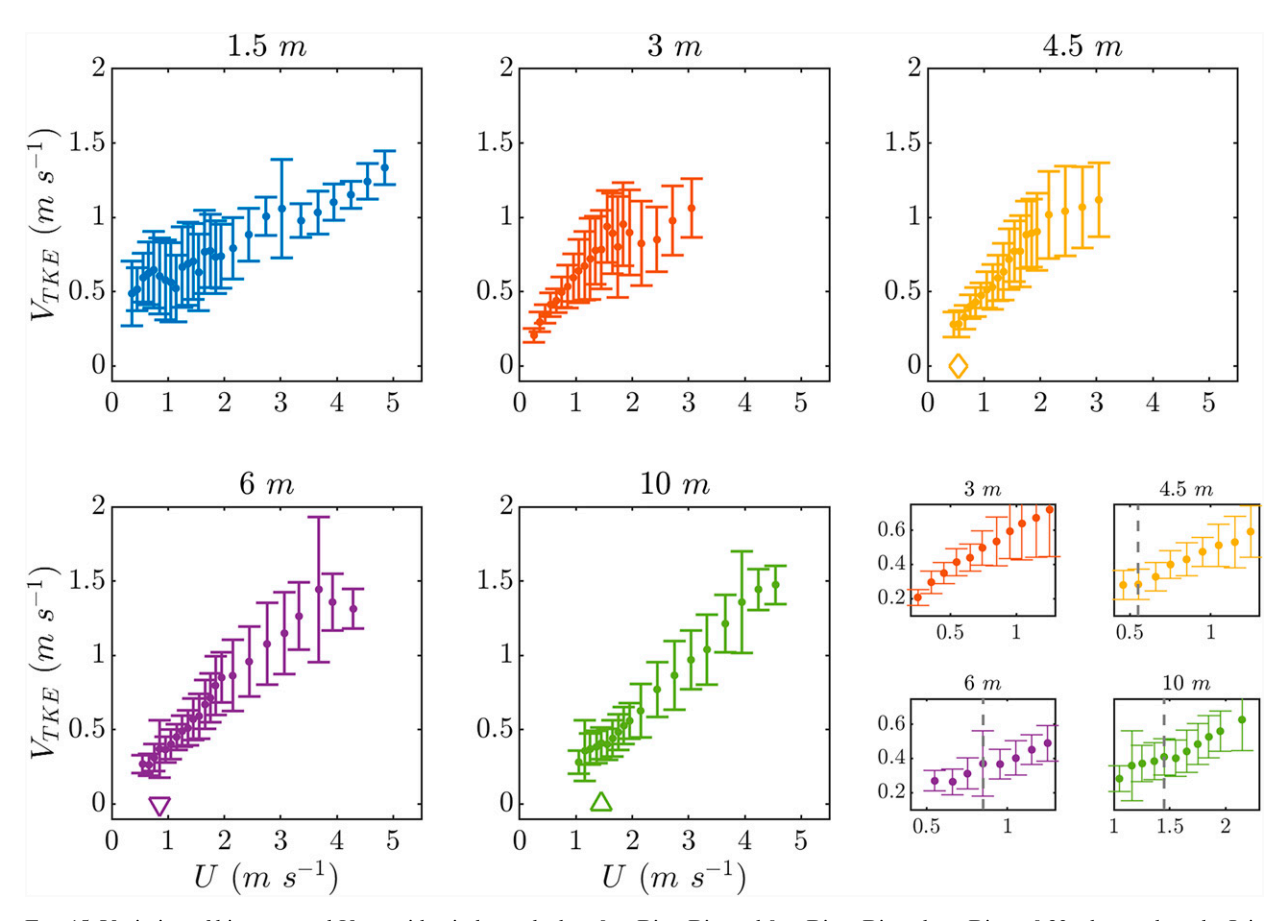


FIG. 15. Variation of bin-averaged $V_{\rm TKE}$ with wind speed when $0 < {\rm Ri} \le {\rm Ri}_{\rm cr}$ and $0 < {\rm Ri}_f \le {\rm Ri}_{\rm cr}$, where ${\rm Ri}_{\rm cr} = 0.23$, observed on the Init tower for preharvest nights. Bins with fewer than 20 observations were excluded.

included for reference. The postharvest roughness length of 0.05 m estimated for the SAVANT Init tower was still higher than the CASES-99 value of 0.027 m. The roughness length for the BLLAST campaign was approximated to be 0.1 m, as based on the topography and land coverage. At any given height, the threshold wind speed reduced with increased roughness length, except for SHEBA whose threshold wind speed at 5.1 m was 2.3 m s⁻¹, which is less than the threshold wind speed at a similar height for CASES-99.

The effect of roughness is more evident in HOST formulation in terms of reduced V_s for observation heights above the crop layer and absence of V_s for heights within the crop layer. On the other hand, the regime classification worked well for identifying the time periods that agree well with the MOST flux–gradient relationships. Also, for regime 3, the very stable regime, the $V_{\rm TKE}$ magnitude remained low and wind speeds observed were weak. It can be debated whether $V_{\rm TKE}$ variation in regime 3 could be considered as HOST because a threshold wind speed is not identifiable for such weak winds.

5. Summary

Stable boundary layer observations during the SAVANT field campaign were used to test and better understand the HOST

and MOST relationships identified in previous studies. The SAVANT campaign resulted in a dataset containing turbulence observations up to 10-20 m along a shallow gully during pre- and postharvest periods. The nondimensional shear ϕ_m followed the MOST similarity relation when $Ri < Ri_{cr}$ and $Ri_f < Ri_{cr}$, with $Ri_{cr} = 0.23$. Two additional regimes were identified in the range $Ri < Ri_{cr}$ and $Ri_f < Ri_{cr}$, in which the TKE variation with stability parameter differed. When $0 < Ri \le 0.1$ and $0 < Ri_f \le 0.1$, TKE decreased sharply with increasing stability and ζ varied from near-neutral to weakly stable. At $Ri = Ri_f = 0.1$, the vertical velocity variance scaled by the TKE reached a maximum value and thereafter decreased for higher Ri and Rif values. The velocity standard deviations scaled by the friction velocity followed a constant value up to Ri = 0.1 and Ri_f = 0.1 and increased when Ri > 0.1 and $Ri_f > 0.1$. For $0.1 < Ri \le Ri_{cr}$ and $0.1 < Ri_f \le Ri_{cr}$, the rate of change of TKE with stability decreased and the TKE reached a quasi-steady value and the stability in this regime varied from weakly stable to stable. When Ri and $Ri_f > Ri_{cr}$ the TKE did not relate to the stability and ζ in this regime varied between nearneutral to strongly stable.

The bin-averaged turbulence intensity ($V_{\rm TKE}$) relation with mean wind speed at different heights on the initiation tower was tested against the HOST theory (Sun et al. 2012). For postharvest nights, and for stable periods that Ri and Ri_f are

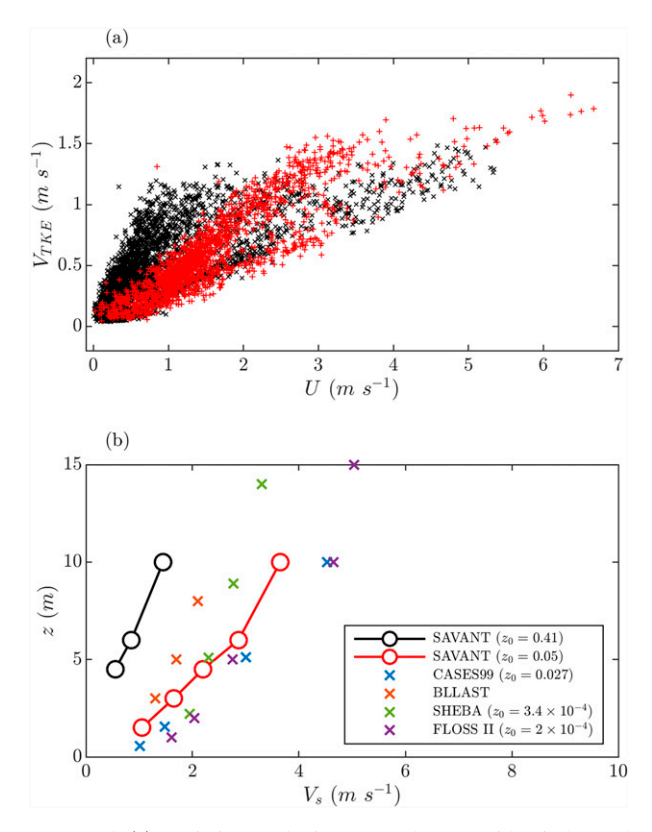


FIG. 16. (a) Variation of 5-min-averaged $V_{\rm TKE}$ with wind speed when $0 < {\rm Ri} \le {\rm Ri}_{\rm cr}$ and $0 < {\rm Ri}_f \le {\rm Ri}_{\rm cr}$, where ${\rm Ri}_{\rm cr} = 0.23$, observed on initiation tower at 4.5 m for preharvest (black times signs; $z_0 = 0.41$) and postharvest nights (red plus signs; $z_0 = 0.05$). (b) Variation of V_s (threshold wind speed) with height compared with the CASES-99 data from Sun et al. (2012), BLLAST data from Yus-Díez et al. (2019), SHEBA data from Chechin (2021), and the second phase of the Fluxes Over Snow Surfaces (FLOSS-II) data from Acevedo et al. (2016).

less than the critical Richardson number ($Ri_{cr} = 0.23$), two distinctive turbulence intensity regimes were observed that can be separated based on a threshold wind speed V_s . When the winds were lower than this threshold wind speed, the turbulence intensity remained approximately constant. Once the winds were stronger than V_s , turbulence intensity increased linearly with the wind speed. The threshold wind speed value increased with height in a way that is similar to that reported using the CASES-99 dataset. The magnitude of the threshold wind speed at all the heights on the initiation tower were lower than those reported for CASES-99 in Sun et al. (2012). For periods with Ri and $Ri_f > 0.23$, the turbulence remained low over a range of very weak to weak wind speeds. No significant top-down turbulence events were observed at initiation tower during SAVANT. This could be due to the absence of elevated turbulence caused by gravity waves, low-level jets, Kelvin-Helmholtz instabilities, or such. Another possibility could be the top-down turbulence transport is not strong enough to reach lower levels close to the ground (z < 10 m), one such event was identified during BLLAST campaign (Yus-Díez et al. 2019, see their Fig. 12). For preharvest nights,

to investigate the effect of roughness, we used the daytime near-neutral periods to estimate the zero displacement and roughness heights near the initiation tower, which were found to be 1.7 and 0.41 m, respectively. The ϕ_m followed the MOST similarity relation for preharvest periods when Ri < Ri_{cr} and $Ri_f < Ri_{cr}$. For observations above the crop layer, additional roughness during preharvest periods reduced the threshold wind speed required to enhance the TKE. The roughness characteristics present at SAVANT site pose a unique challenge. The terrain relief within 1-km radius was about 20 m, and, more important, the crop layer started approximately 100 m west of the observation tower. The dominant winds during preharvest period were from west. The roughness characteristics of corn and soybean crop presented in this study are more common in the agricultural fields across the midwestern part of the United States.

Acknowledgments. Funding for this study was provided from NSF Awards 1733877 and 1733746 and the Illinois State Water Survey at the University of Illinois at Urbana—Champaign. The authors thank UCAR staff and several students who participated during SAVANT and are responsible for generating the dataset. Opinions expressed are those of the authors and not necessarily those of the Illinois State Water Survey, the Prairie Research Institute, or the University of Illinois. The authors declare that there is no conflict of interest.

Data availability statement. All data used in this study are openly available from the NCAR/EOL SAVANT data archive (https://doi.org/10.26023/NKWR-EYWS-5J0W).

REFERENCES

Acevedo, O. C., L. Mahrt, F. S. Puhales, F. D. Costa, L. E. Medeiros, and G. A. Degrazia, 2016: Contrasting structures between the decoupled and coupled states of the stable boundary layer. *Quart. J. Roy. Meteor. Soc.*, 142, 693–702, https://doi.org/10.1002/qj.2693.

Anderson, P. S., 2009: Measurement of Prandtl number as a function of Richardson number avoiding self-correlation. *Bound.-Layer Meteor.*, 131, 345–362, https://doi.org/10.1007/s10546-009-9376-4.

Baas, P., G. J. Steeneveld, B. J. H. Van De Wiel, and A. A. M. Holtslag, 2006: Exploring self-correlation in flux-gradient relationships for stably stratified conditions. *J. Atmos. Sci.*, 63, 3045–3054, https://doi.org/10.1175/JAS3778.1.

Babić, K., and M. W. Rotach, 2018: Turbulence kinetic energy budget in the stable boundary layer over a heterogeneous surface. *Quart. J. Roy. Meteor. Soc.*, **144**, 1045–1062, https:// doi.org/10.1002/qj.3274.

Banta, R. M., L. Mahrt, D. Vickers, J. Sun, B. B. Balsley, Y. L. Pichugina, and E. J. Williams, 2007: The very stable boundary layer on nights with weak low-level jets. *J. Atmos. Sci.*, 64, 3068–3090, https://doi.org/10.1175/JAS4002.1.

Blumen, W., R. Banta, S. P. Burns, D. C. Fritts, R. Newsom, G. S. Poulos, and J. Sun, 2001: Turbulence statistics of a Kelvin-Helmholtz billow event observed in the night-time boundary layer during the Cooperative Atmosphere-Surface

- Exchange Study field program. *Dyn. Atmos. Oceans*, **34**, 189–204, https://doi.org/10.1016/S0377-0265(01)00067-7.
- Bonin, T. A., W. G. Blumberg, P. M. Klein, and P. B. Chilson, 2015: Thermodynamic and turbulence characteristics of the southern Great Plains nocturnal boundary layer under differing turbulent regimes. *Bound.-Layer Meteor.*, 157, 401–420, https://doi.org/10.1007/s10546-015-0072-2.
- Businger, J. A., J. C. Wyngaard, and Y. Izumi, 1971: Flux profile relationships in the atmospheric surface layer. J. Atmos. Sci., 28, 181–189, https://doi.org/10.1175/1520-0469(1971)028<0181: FPRITA>2.0.CO;2.
- Chamecki, M., N. L. Dias, and L. S. Freire, 2018: A TKE-based framework for studying disturbed atmospheric surface layer flows and application to vertical velocity variance over canopies. *Geophys. Res. Lett.*, 45, 6734–6740, https://doi.org/10. 1029/2018GL077853.
- Chechin, D., 2021: On the u_★-U relationship in the stable atmospheric boundary layer over Arctic Sea Ice. Atmosphere, 12, 591, https://doi.org/10.3390/atmos12050591.
- Chenge, Y., and W. Brutsaert, 2005: Flux-profile relationships for wind speed and temperature in the stable atmospheric boundary layer. *Bound.-Layer Meteor.*, 114, 519–538, https:// doi.org/10.1007/s10546-004-1425-4.
- Cionco, R. M., 1972: A wind-profile index for canopy flow. Bound. Layer Meteor., 3, 255–263, https://doi.org/10.1007/BF02033923.
- Cuxart, J., and Coauthors, 2000: Stable Atmospheric Boundary-Layer Experiment in Spain (SABLES 98): A report. *Bound.-Layer Meteor.*, 96, 337–370, https://doi.org/10.1023/A:1002609509707.
- Dyer, A. J., 1974: A review of flux-profile relationships. Bound.-Layer Meteor., 7, 363–372, https://doi.org/10.1007/BF00240838.
- Freire, L. S., M. Chamecki, E. Bou-Zeid, and N. L. Dias, 2019: Critical flux Richardson number for Kolmogorov turbulence enabled by TKE transport. *Quart. J. Roy. Meteor. Soc.*, 145, 1551–1558, https://doi.org/10.1002/qj.3511.
- Fuentes, J. D., and Coauthors, 2016: Linking meteorology, turbulence, and air chemistry in the Amazon rain forest. *Bull. Amer. Meteor. Soc.*, 97, 2329–2342, https://doi.org/10.1175/BAMS-D-15-00152.1.
- Garratt, J. R., 1994: The atmospheric boundary layer. *Earth-Sci. Rev.*, **37**, 89–134, https://doi.org/10.1016/0012-8252(94)90026-4.
- Grachev, A. A., C. W. Fairall, P. O. G. Persson, E. L. Andreas, and P. S. Guest, 2005: Stable boundary-layer scaling regimes: The SHEBA data. *Bound.-Layer Meteor.*, 116, 201–235, https://doi.org/10.1007/s10546-004-2729-0.
- ——, E. L. Andreas, C. W. Fairall, P. S. Guest, and P. O. G. Persson, 2007: SHEBA flux–profile relationships in the stable atmospheric boundary layer. *Bound.-Layer Meteor.*, 124, 315–333, https://doi.org/10.1007/s10546-007-9177-6.
- —, —, —, and —, 2013: The critical Richardson number and limits of applicability of local similarity theory in the stable boundary layer. *Bound.-Layer Meteor.*, **147**, 51–82, https://doi.org/10.1007/s10546-012-9771-0.
- Hiscox, A. L., and Coauthors, 2019: SAVANT: A field campaign for the stable boundary layer. *Ninth Symp. on Lidar Atmo*spheric Applications, Phoenix, AZ, Amer. Meteor. Soc., 1.6, https://ams.confex.com/ams/2019Annual/meetingapp.cgi/Paper/ 353593.
- Howard, L. N., 1961: Note on a paper of John W. Miles. J. Fluid Mech., 10, 509–512, https://doi.org/10.1017/S0022112061000317.
- Klipp, C. L., and L. Mahrt, 2004: Flux–gradient relationship, self-correlation and intermittency in the stable boundary layer. Quart. J. Roy. Meteor. Soc., 130, 2087–2103, https://doi.org/10.1256/qj.03.161.

- LeMone, M. A., and Coauthors, 2019: 100 years of progress in boundary layer meteorology. A Century of Progress in Atmospheric and Related Sciences: Celebrating the American Meteorological Society Centennial, Meteor. Monogr., No. 59, Amer. Meteor. Soc., https://doi.org/10.1175/AMSMONOGRAPHS-D-18-0013.1.
- Liang, J., L. Zhang, Y. Wang, X. Cao, Q. Zhang, H. Wang, and B. Zhang, 2014: Turbulence regimes and the validity of similarity theory in the stable boundary layer over complex terrain of the Loess Plateau, China. J. Geophys. Res., 119, 6009– 6021, https://doi.org/10.1002/2014JD021510.
- Lothon, M., and Coauthors, 2014: The BLLAST field experiment: Boundary-layer late afternoon and sunset turbulence. *Atmos. Chem. Phys.*, **14**, 10 931–10 960, https://doi.org/10.5194/acp-14-10931-2014.
- Mahrt, L., 1998: Nocturnal boundary-layer regimes. *Bound.-Layer Meteor.*, 88, 255–278, https://doi.org/10.1023/A:1001171313493.
- —, 2014: Stably stratified atmospheric boundary layers. Annu. Rev. Fluid Mech., 46, 23–45, https://doi.org/10.1146/annurev-fluid-010313-141354.
- —, and D. Vickers, 2002: Contrasting vertical structures of nocturnal boundary layers. *Bound.-Layer Meteor.*, **105**, 351–363, https://doi.org/10.1023/A:1019964720989.
- —, —, R. Nakamura, M. R. Soler, J. Sun, S. Burns, and D. H. Lenschow, 2001: Shallow drainage flows. *Bound.-Layer Meteor.*, **101**, 243–260, https://doi.org/10.1023/A:1019273314378.
- —, C. Thomas, S. Richardson, N. Seaman, D. Stauffer, and M. Zeeman, 2013: Non-stationary generation of weak turbulence for very stable and weak-wind conditions. *Bound.-Layer Meteor.*, 147, 179–199, https://doi.org/10.1007/s10546-012-9782-x.
- —, J. Sun, and D. Stauffer, 2015: Dependence of turbulent velocities on wind speed and stratification. *Bound.-Layer Meteor.*, 155, 55–71, https://doi.org/10.1007/s10546-014-9992-5.
- Monin, A. S., and A. M. Obukhov, 1954: Basic laws of turbulent mixing in the surface layer of the atmosphere. Tr. Geofiz. Inst., Akad. Nauk SSSR, 24, 163–187.
- NCAR/EOL In-Situ Sensing Facility, 2021: NCAR/EOL ISFS Surface Meteorology and Flux Products, 5-minute, geographic coordinate, and tilt corrected winds, version 2.0. NCAR/ UCAR, accessed 15 March 2021, https://doi.org/10.26023/ NKWR-EYWS-5J0W.
- Optis, M., A. Monahan, and F. C. Bosveld, 2014: Moving beyond Monin–Obukhov similarity theory in modelling wind-speed profiles in the lower atmospheric boundary layer under stable stratification. *Bound.-Layer Meteor.*, 153, 497–514, https://doi. org/10.1007/s10546-014-9953-z.
- Pahlow, M., M. B. Parlange, and F. Porté-Agel, 2001: On Monin– Obukhov similarity in the stable atmospheric boundary layer. *Bound.-Layer Meteor.*, 99, 225–248, https://doi.org/10.1023/A: 1018909000098.
- Poulos, G. S., and Coauthors, 2002: CASES-99: A comprehensive investigation of the stable nocturnal boundary layer. *Bull. Amer. Meteor. Soc.*, 83, 555–582, https://doi.org/10.1175/1520-0477(2002)083<0555:CACIOT>2.3.CO;2.
- Sorbjan, Z., 2010: Gradient-based scales and similarity laws in the stable boundary layer. *Quart. J. Roy. Meteor. Soc.*, **136**, 1243– 1254, https://doi.org/10.1002/qj.638.
- —, and A. A. Grachev, 2010: An evaluation of the flux–gradient relationship in the stable boundary layer. *Bound.-Layer Meteor.*, 135, 385–405, https://doi.org/10.1007/s10546-010-9482-3.
- Sun, J., 1999: Diurnal variations of thermal roughness height over a grassland. *Bound.-Layer Meteor.*, 92, 407–427, https://doi. org/10.1023/A:1002071421362.

- —, L. Mahrt, R. M. Banta, and Y. L. Pichugina, 2012: Turbulence regimes and turbulence intermittency in the stable boundary layer during CASES-99. *J. Atmos. Sci.*, 69, 338–351, https://doi. org/10.1175/JAS-D-11-082.1.
- —, D. H. Lenschow, M. A. LeMone, and L. Mahrt, 2016: The role of large-coherent-eddy transport in the atmospheric surface layer based on CASES-99 observations. *Bound.-Layer Meteor.*, 160, 83–111, https://doi.org/10.1007/s10546-016-0134-0.
- ——, E. S. Takle, and O. C. Acevedo, 2020: Understanding physical processes represented by the Monin–Obukhov bulk formula for momentum transfer. *Bound.-Layer Meteor.*, 177, 69–95, https://doi.org/10.1007/s10546-020-00546-5.
- Vickers, D., and L. Mahrt, 2003: The cospectral gap and turbulent flux calculations. *J. Atmos. Oceanic Technol.*, **20**, 660–672, https://doi.org/10.1175/1520-0426(2003)20<660:TCGATF>2. 0.CO:2.

- —, and —, 2004: Evaluating formulations of stable boundary layer height. J. Appl. Meteor., 43, 1736–1749, https://doi.org/ 10.1175/JAM2160.1.
- —, and —, 2006: A solution for flux contamination by mesoscale motions with very weak turbulence. *Bound.-Layer Meteor.*, 118, 431–447, https://doi.org/10.1007/s10546-005-9003-y.
- Wyngaard, J. C., 2010: Turbulence in the Atmosphere. Cambridge University Press, 393 pp.
- Yagüe, C., S. Viana, G. Maqueda, and J. M. Redondo, 2006: Influence of stability on the flux-profile relationships for wind speed, Φm, and temperature, Φh, for the stable atmospheric boundary layer. Nonlinear Processes Geophys., 13, 185–203, https://doi.org/10.5194/npg-13-185-2006.
- Yus-Díez, J., M. Udina, M. R. Soler, M. Lothon, E. Nilsson, J. Bech, and J. Sun, 2019: Nocturnal boundary layer turbulence regimes analysis during the BLLAST campaign. *Atmos. Chem. Phys.*, 19, 9495–9514, https://doi.org/10.5194/acp-19-9495-2019.